A High Stability Optical Shadow Sensor With Applications for Precision Accelerometers

Steven G. Bramsiepe, David Loomes, Richard P. Middlemiss,
Douglas J. Paul, *Senior Member, IEEE*, and Giles D. Hammond

***Abstract*— Displacement sensors are found in a variety of applications including gravitational wave detectors, precision metrology, tissue imaging, gravimeters, microscopy, and environmental monitoring. Most of these applications benefit from the use of displacement sensors that offer both high precision and stability. This is particularly the case for gravimetry where measurements are often taken over multi-day timescales. In this paper we describe a custom-built microcontroller-based displacement sensor that has been utilized in a micro-electromechanicalsystem gravimeter. The system runs off battery power and is low-cost, portable, and lightweight. Using an optical shadow sensor technique, and by designing a digital lock-in amplier based around a dsPIC33 microcontroller, we demonstrate a displacement sensitivity of 10 nm/Hz down to 300 s, and an rms sensitivity of 1 nm over timescales of one day. The system also provides real time monitoring/control of temperature, using an AD7195 ratiometric bridge to provide mK control of three separate PT100 sensors. Furthermore, a tilt sensor conditioning circuit is incorporated to drive a pair of electrolytic tilt sensors, resulting in the ability to monitor 2 axis tilt at the level of 1 microradian over approximately 1 day. The sensor system described is thus multifunctional and capable of being incorporated into precision accelerometers/gravimeters, or indeed other applications where long term displacement/temperature monitoring is necessary.**

***Index Terms*— Shadow sensor, displacement sensor, low noise, gravimeter, gravimetry, low noise electronics, lock-in amplifier, digital lock-in amplifier, digital filters.**

I. Introduction

DISPLACEMENT sensors have many applications, one such application in research is the use of a shadow sensor in Advanced LIGO (aLIGO), the ground-based interferometric gravitational wave detector [1]. Displacement sensors also have industrial applications such as environmental monitoring [2], biomedical sensing [3]–[5], microscopy [6], [7], the manufacturing industry [8], [9], hydraulic device position monitoring [10] and gravimeters [11].

Manuscript received January 12, 2018; revised February 21, 2018 and February 25, 2018; accepted March 6, 2018. Date of publication March 21, 2018; date of current version April 23, 2018. This work was supported by EPSRC QuantIC under Grant EP/MO1326X/1. The work of S. G. Bramsiepe was supported by EPSRC under Grant EP/L016753/1. The associate editor coordinating the review of this paper and approving it for publication was Dr. Ferran Reverter. *(Corresponding author: Steven G. Bramsiepe.)*

S. G. Bramsiepe, R. P. Middlemiss, and G. D. Hammond are with the SUPA School of Physics and Astronomy, University of Glasgow, Glasgow G12 8UU, U.K. (e-mail: s.bramsiepe.1@research.gla.ac.uk; richard.middlemiss@glasgow.ac.uk; giles.hammond@glasgow.ac.uk).

D. Loomes is with DaLEK Software Ltd., Glasgow G61 1EJ, U.K. (e-mail: david@xoomspeed.com).

D. J. Paul is with the School of Engineering, University of Glasgow, Glasgow G12 8LT, U.K. (e-mail: douglas.paul@glasgow.ac.uk).

Digital Object Identifier 10.1109/JSEN.2018.2818066

Recently a Micro-electro Mechanical System (MEMS) gravimeter has been fabricated and tested, demonstrating the possibility for small, low-cost and lightweight gravimeters [11]–[13]. The MEMS chip is manufactured from a single piece of silicon, and is comprised of a proof mass suspended from microscopic springs (or flexures). The gravimeter requires a displacement sensor that is stable over timescales of days with sensitivities of nanometers over this period. The MEMS also requires the use of temperature control, tilt monitoring and conditioning electronics, whilst also fitting the criteria of being low-cost, lightweight and portable. For example, to measure a useful accelerations of 40 μGal,[1] a displacement sensitivity of ≤ 2.5 nm is required for a 2 Hz resonator.

The displacement of the MEMS proof mass is measured using the lock-in technique [14] with a shadow sensor such as the one used in aLIGO [1]. Although the shadow sensor presented by N. A. Lockerbie et al has very good performance, 69 ± 13 pm$_{rms}/\sqrt{\text{Hz}}$, this performance is at high frequency (500 Hz) in order to monitor violin modes of the suspension fibres. Our application requires stability over day timescales in order to sense earth tides. There is no available system which provides nanometer displacement stability over this time period, that can also monitor temperatures at the mK level, and provide tilt readout better than 1 μrad. The system also needs to be portable and run off battery power. Since the meeting of these criteria was essential for this application, significant development of the electronic circuitry was required (a picture of the system can be seen in figure 1a and the electronics board in figure 1b). The shadow sensor operates by illuminating the proof mass (or any object) using an LED. This light beam then causes a shadow to fall on the photodiodes, where, if the object moves, so does the shadow, thus causing a change in photocurrent from the photodiodes. An example of the shadow sensor used in this papers system can be seen in figure 2. Lock-in amplifiers are a well used technique and are commonly used to remove $1/f$ noise by modulating a given signal at a higher frequency before demodulating, which has the effect of moving $1/f$ to higher frequency. This then allows the use of a low-pass filter to remove the initial $1/f$ noise [14].

To obtain the required functionality for our application, a suite of electronics is required to: modulate and demodulate the LED and signal respectively; measure and control the temperatures via use of digital to analogue converters (DACs),

[1] 1 Gal $\equiv$ 10 mm s^{-2} $\approx$ 1 mg

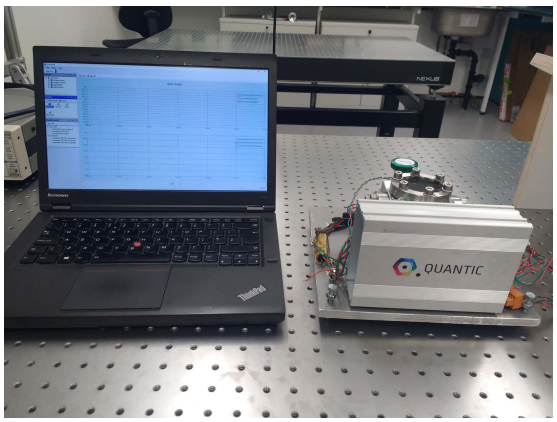

(a)

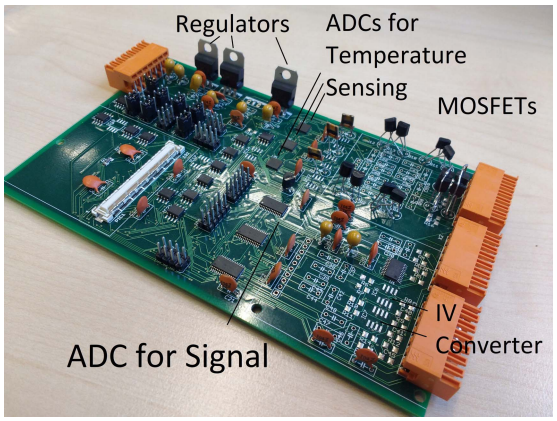

(b)

Fig. 1. (a) A picture of the full system including laptop to read off the data. Small vacuum cube can be seen behind the electronics board enclosure on the right. The system is powered by two 7.4 V lithium ion batteries. (b) A picture of the 4 layer custom electronics board designed and tested. The two specialised analogue to digital converters (ADCs) are highlighted. AD7195s are used for temperature sensing and an ADS1248 is used to sample a modulated signal.

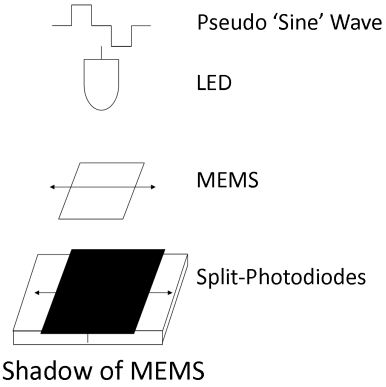

Fig. 2. Illustration of the Shadow Sensor Technique. LED illuminates a moving MEMS that casts a shadow over a split photodiode that takes the difference in intensities of the two photodiodes. This allows large gains during amplification.

analogue to digital converters (ADCs) and heaters; convert the photocurrents to a voltage (IV converter); and compute digital filters. The temperature control is needed as the system is sensitive to temperature changes, both in the LED and the MEMS itself. Temperature changes effect the Young's modulus of the silicon and due to thermal expansion, for example, a 1 K change in temperature would result in a 1.6 μm displacement (the equivalent of 25 μGal per mK [11]). Therefore the temperature of the MEMS needed to be controlled to within ± 2 mK to obtain the necessary acceleration sensitivity.

To utilise the small, lightweight nature of the MEMS, the electronics surrounding the device from Middlemiss *et al.* [11] had to be miniaturised. Many of the individual pieces of electronic equipment used in this original system cost in excess of £1000 each, therefore, using any such electronic equipment would limit our ability to achieve the main objective of creating a low-cost, lightweight and portable system. The objective for this project, therefore, was to reduce an entire 19" rack of electronics down to a portable, battery-powered system whilst maintaining the 2.5 nm sensitivity (and other functionality discussed above). There were no off-the-shelf electronics that had all the requirements necessary, so a custom board had to be designed. The electronics board (seen in figure 1b) would utilise a micro-processor to communicate with each of the components and compute digital filters.

Since the MEMS is measuring the force of gravity exerted on a mass on a spring system, tilt becomes an important variable to measure. If the angle to the force of gravity changes, the device is no longer experiencing the same gravitational acceleration resulting in change of signal. The gravitational acceleration on the device is given by, $g\cos\theta$ where θ is the angle to the vertical. Therefore it was important to design the electronics board to be able to measure this tilt.

It was noted that to miniaturise the system, a small and cost effective lock-in amplifier would have to be designed and created. It was observed from [15]–[20] that digital lock in amplifiers could have the necessary performance for the gravimeter system and could even be implemented in low cost micro-controllers [21], [22] such as the dsPIC33E [23], [24]. Circuitry was therefore designed in which a micro-controller demodulates the signal from the photodiodes (unlike the previous system [11], which used an analogue lock-in amplifier from Femto (LIA-MV(D)-200-L [25])).

In this paper we present the results of the micro-controller based electronics board capable of displacement sensitivities of 0.6 nm in an integration time of 1000 s. Furthermore, the displacement sensor can maintain its sensitivity over timescales of a day or more by controlling temperatures to ± 2 mK and monitoring tilt to within ± 1 μrad. The system developed has allowed the MEMS gravimeter to be successfully taken into the field for gravimetry measurements [26]. Although the sensing system was designed for use in a for use in a MEMS gravimeter, the system's high stability and accuracy mean that it could be applied in other precision sensing applications.

II. Electronics Board

The vision of a low cost, lightweight and portable displacement sensor for use in a MEMS gravimeter required the design

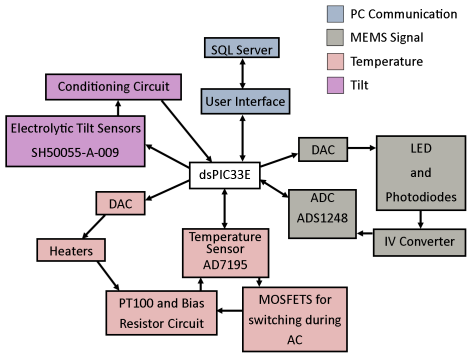

Fig. 3. A block diagram outlining the functionality of the custom electronics board used to make low noise displacement measurements of a MEMS gravimeter. The block diagram is comprised of four discrete sections and are the processes involved in: communicating with the PC, measurements of the MEMS, measurements of temperature and its control and measurements of tilt.

and testing of a custom electronics board. This was because an integrated system which combined the functionality required to make useful gravity measurements did not exist. The MEMS required the ability to: source a stable modulated drive for an LED to be used in the shadow sensor; convert the low currents from a split photodiode setup into a usable digital signal via use of a transimpedance amplifier and analogue to digital converter; measure and control temperatures via the use of a ratiometric resistance measurement and a proportional, integral and derivative (PID) controller; monitor tilt allowing regression if necessary; compute digital filters including finite impulse response (FIR) filters and decimations. The board would also require the data to be accessible in real time and allow settings to be changed also in real time. Figure 3 shows a block diagram of the necessary functions of the electronics system.

The electronics board was unified by a Microchip dsPIC33E micro-processor. This dsPIC is used to communicate with the electronics on the electronics board and communicate with a custom user interface (UI) on a laptop or desktop using a SQL Server framework database. The micro-controller would check during each loop for a valid connection to a computer and database, then, several data packets containing the latest information on both the analogue and digital inputs and outputs are sent to the computer and database. The user interface then communicates with the database to collect the latest values/settings on the UI. This custom UI also has the ability to plot graphs in real time and take logs for future use. It was, however, limited to refreshing values at a rate of $0.5 \rightarrow 30$ Hz due to limitations in communicating with the database. This 30 Hz is a soft limit and could probably be exceeded, however, it was found to be unnecessary since the decimation of the data reduces the data rate below this level.

III. Shadow Sensor

The displacement of the proof mass is measured using a shadow sensor combined with a lock-in amplifier. In the shadow sensor, the MEMS proof mass is illuminated with an LED, creating a shadow on the photodiodes (as seen in figure 2). Here the LED is diffused through a piece of sapphire to smooth any features due to the beam profile. The spot size on the MEMS is approximately 12 mm and slightly larger on the two 5×5 mm planar photodiodes. This photo-current is then converted to a voltage and sampled via an ADC. Several forms of shadow sensor exist. In this system, two photodiodes in a differential setup [11] are used (as seen in figure 2) to measure in 1 dimension. There does, however, exists a version using a quadrant arrangement of photodiodes [27] and a 3D arrangement [28] but due to the proof mass being constrained in one dimension and that we are only interesting in vertical gravity, the simpler 1D case with two photodiodes is sufficient. The photodiodes are operated in a photovoltaic mode to reduce the dark noise. The electronics convert the photocurrent from the photodiodes to a voltage using a current to voltage converter. This current to voltage converter, or, transimpedance amplifier uses a LT1793a low input bias JFET. The amplfifier contains a low pass filter (RC network) with a gain of 2×10^6. The low pass was designed to have a cut off frequency at ≈ 2300 Hz even though the sampling frequency of the ADC was much lower (640 Hz). Since the RC cutoff is higher than that of the Nyquist frequency of the ADC sampling, aliasing would occur where higher frequency noise "wraps" into the lower frequencies which are still within the Nyquist limit. The waveform which was used was a "pseudo-sine" which is similar to a square wave but instead with three distinct levels, low, zero and high, i.e. a sine wave with 4 points per cycle (seen in figure 2). If the cut off frequency was lower, rounding was observed in the output due to the higher frequency components being attenuated. The ADS1248 samples an input between 0 and 3 V and cannot accept any input that is below ground. This is why 1.5 V was summed onto each side of the input before going to the ADS (this fully differential measurement can bee seen on page 29 of the datasheet [29]). The DC bias was summed on using a TL071 in a non inverting summing configuration. The current source ensures that a constant current is being supplied for a given control voltage (rather than the system draw as much current as it needs). In an ideal case where the proof mass is perfectly centered on the shadow sensor, zero signal would be the output and, any changes in the LED would be cancelled as the variations are common in both the photodiodes such as relative intensity noise. An advantage of using a differential setup (also known as a split photodiode) is that large gains can be realised due to the currents having been subtracted before the transimpedance amplifier stage. If, instead, a setup required individual amplification of each photodiode before a differential amplifier stage, then the operational amplifiers used are likely to saturate before any subtractions can be carried out. Here we obtain a gain between $(1 \rightarrow 10) \times 10^6$, obtaining a calibration of our signal in Volts of $\approx 20 \times 10^3$ V/m for a drive current of ≈ 11 mA, i.e. we would see a change in signal of ≈ 20 mV for a 1 μm displacement of the proof mass. This calibration in V/m is obtained by moving a small wire or stiff object using a micrometer across the photodiodes by 10 or 50 μm steps and reading of the voltage change on the output.

There are several forms of noise that contribute to the noise in the measured signal (of which Johnson-Nyquist noise and shot noise are examples). An estimation of the shot

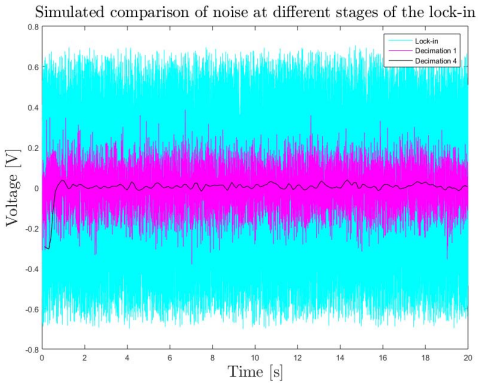

Fig. 4. Figure showing the noise at different stages of the lock-in in a MATLAB simulation of the dsPICs digital filtering. Each decimation stage low-pass filters at $1/8^{\text{th}}$ of the Nyquist frequency allowing a decimation rate of 4:1 per stage. It can be seen that the lock-in output to decimation stage 1 results in a noise reduction factor of $\approx 2 \rightarrow 3$.

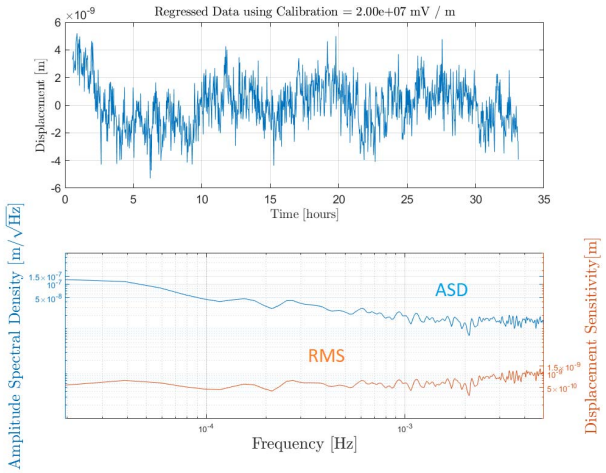

Fig. 5. Output from the shadow sensor over after demodulation, decimation and regression. A linear and 2^{nd} order polynomial regression is used. A total of four decimation stages at a decimation rate of 4:1 per stage is used. Top graph shows the time domain signal over 33 hours, some $1/f$ noise is present with maximum oscillations of 4 nm peak to peak. Lower graph shows the amplitude spectral density (ASD) of this data (left axis) and the rms at that frequency (right axis). The ASD shows a white noise of 10 nm/$\sqrt{\text{Hz}}$ down to 300 s. When integrating the data to 1000 s, a displacement sensitivity of 0.6 nm is obtained seen on the rms.

noise in the system can be obtained by simply covering a single photodiode. The resulting current in this setup is approximately $I = 0.4$ mA from each of the diodes. This can then be combined with equation 1 to obtain a shot noise of 11 pA/$\sqrt{\text{Hz}}$ (or 0.5 nA when multiplying with a bandwidth of $\Delta f = 2300$ Hz).

$$\sigma_i = \sqrt{2 \times q \times I} \tag{1}$$

where q is the fundamental charge of an electron equal to $\approx 1.6 \times 10^{-19}$ C. The shot noise from each of the photodiodes is incoherent and therefore should be added together as such. This gives an overall shot noise of $\sigma_{iT} = \sqrt{2} \times 0.5 \times 10^{-9} \approx 0.7$ nA. This noise is then amplified into voltage noise through the current-to-voltage amplifier. When using a feedback loop with a resistance of 2 MΩ, the current noise becomes a voltage noise, $\sigma_v = \sigma_i T R_f = 0.7 \times 10^{-9} \times 2 \times 10^6 = 1.4$ mV $\equiv 70$ nm. This means 70 nm of noise is on the input of the ADC across a bandwidth of 2300 Hz. The ADC, however, only samples at 640 Hz resulting in aliased noise.

Thermal noise, also known as Johnson-Nyquist noise, originates from random thermal motion of carriers and can be calculated using equation 2 [30].

$$v_n = \sqrt{4 k_B T R \Delta f} \tag{2}$$

Where k_B is Boltzmann's constant and T is temperature ≈ 300 K. A feedback resistor of $R = 2$ MΩ is used, with a bandwidth of $\Delta f = 2300$ Hz, so a thermal noise of 8.7 μV_{rms} can be calculated. This value is several orders of magnitude smaller than the current shot noise and can be ignored as it is not limiting the performance. The ADS1248 also contains noise instrinsic to the inputs. These values are stated on page 21 of the datasheet [29]. For a sampling frequency of 640 Hz, the measurement would have 15.4 effective number of bits (peak to peak), or, 8.6 bits of noise relative to full scale. 8.6 bits of the 3 V is the equivalent of 69.4 μV of noise of the input ($\equiv 34.7$ nm).

Since the dsPIC is demodulating and filtering digitally, a replica of the algorithm was created in MATLAB for simulation purposes. An example of the output from this simulation can be seen in figure 4. The simulation shows that the noise is reduced by a factor of $2 \rightarrow 3$ per decimation stage which is consistent with the cutoff of the filter ($1/8^{th}$ of the Nyquist frequency). The plot on this figure with the least noise shows the output from the fourth (and final) decimation stage. For 1.4 mV of noise on the lockin such as that of the shot noise results in an estimate of 18 μV of noise after the final stage. This is the equivalent of 0.9 nm and is smaller by a factor of $2 \rightarrow 3$ relative to the measured noise seen in figure 5. Likewise the theoretical input noise of the ADC can also be simulated, for 69.4 μV of noise pre-filtering, approximately 3 μV or 0.15 nm of noise is estimated on the output. Experimentally the noise on the input was measured to be 100 nm peak to peak (after being sampled at a bandwidth of 320 Hz). Simulating this noise gives an estimate of 2 nm which matches up well to what is seen at in both the short term noise in figure 5 and the noise on a PGA setting of 1 in figure 6. We believe the excess noise seen in the measurements compared to the theory is possibly due to relative intensity noise (RIN).

IV. Lock-in Amplifier (LIA)

Lock-in amplification is a technique that can remove low frequency (1/f) noise from a measurement. This reduction is achieved by modulating signals at a higher frequency than the experiment, f_M and then demodulating afterwards. This approach obtains noise around the frequency of modulation with the bandwidth chosen by the low pass filter used after the demodulation.

A. Digital Lock-in Amplifiers

The electronics board creates a modulated drive signal in a unique way relative to most other systems. The DAC (TLV5616 [31]) that is used for the drive signal is only

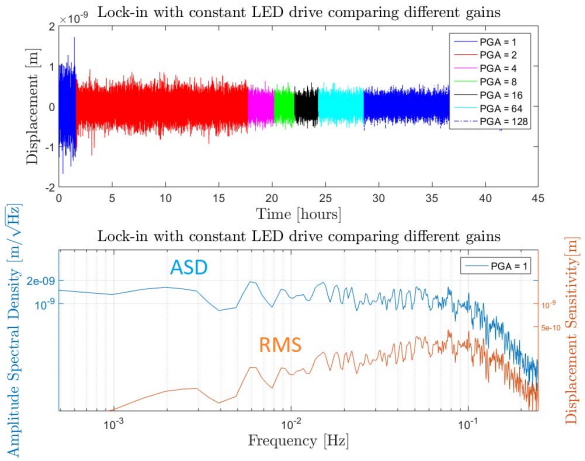

Fig. 6. Output from the 4th decimation step of the lock-in without any fixed flag or modulation on the LED. It shows initially a decreasing noise as the gain on the ADC increases. Should be noted that the peak to peak noise is lower than that when modulating the LED implying the system is limited by the LED. The lower graph shows the amplitude spectral density at the PGA of 1 and the amplitude once multiplied by the frequency.

changed when a sample is recorded by the ADS1248 [29]. Once the micro-controller receives an updated value from the ADS1248, the firmware puts the ADS1248 to sleep and then changes the output of the DAC. After a pre-programmable number of clock cycles, the micro-controller then awakens the ADS1248 and starts it converting a sample. This process is then repeated. The pre-programmable delay is used to ensure that the ADS1248 samples once the signal has settled to a new value. The modulated signal is in the form of a 'pseudo-sine wave' – a sine wave with only 4 points per cycle, 0, 1, 0, −1 (figure 2). Since the change of the DAC being used for the "pseudo-sine" and therefore modulation frequency are locked to when the ADS1248 samples, using 4 points per cycle has an advantage as the less points per cycle the higher the modulation frequency. This signal still contains the necessary frequency information for demodulating to a DC level and was chosen over a conventional square wave as it gives information on both the in-phase and out of phase components of the signal. To allow the photodiode/low-pass filters to settle, a 400 μs delay was introduced. This delay had the effect of reducing the modulation frequency from 160 Hz to 120 Hz. The settling time of the system was observed on an oscilloscope to obtain the delay. Even though the ADS1248 can sample up to 2 kHz, the sampling rate was chosen to be 640 Hz since the input referred noise increases with the sampling frequency (as seen on page 21 of its datasheet [29]). Though the increase in sampling rate would increase the modulation frequency as they are locked together, it would not give better noise relative to the increased input noise.

Once the signal is demodulated, the micro-controller filters the data using a finite impulse response (FIR) filter [32]. This takes advantage of the dsPIC's specialised digital signal processing (DSP) engine that can multiply two data registers, add the result to an accumulator, fetch the next data words to the data registers and update these data registers in two clock cycles [33]. This engine block allows many different variables each to have their own decimation stage, allowing variables to be chosen for filtering and decimation, without slowing down the performance of the dsPIC. The filter used for decimating is a custom low pass with a cut off frequency at $1/8^{th}$ of the sampling frequency, allowing a decimation factor rate of 4:1 without running into aliasing [32].

The upper plot of figure 5 shows the typical rms displacement of a fixed flag system measured over more than a day after it has been demodulated, decimated and regressed using a linear and 2^{nd} order polynomial regression. The lower graph shows the amplitude spectral density (ASD) and the root mean square (RMS) at that frequency. The ASD in figure 5 shows a sensitivity of 10 nm/$\sqrt{\text{Hz}}$ down to 300 s. When averaging the data over the 1000 s for example, a displacement sensitivity of 0.6 nm over timescales of days is obtained. Averaging to 10000 s only decreases the noise by a factor of 2 due to the $1/f$ noise. Figure 6 shows the rms noise when the LED is not being modulated but is on at a constant output. It shows a noise peak to peak of 2 nm with no low frequency drift (compared to 4 nm short term noise when the LED is modulated). Comparing the two figures it can be observed that modulating the LED increases noise across all frequencies and in particular introduces $1/f$ noise which limits the benefit from averaging. This would imply the system is normally limited by the LED. The shadow sensor originally used in Middlemiss *et al.* [11] obtained a sensitivity of 2.5 nm/$\sqrt{\text{Hz}}$ at 1 Hz where here we obtain a sensitivity of 10 nm/$\sqrt{\text{Hz}}$. Though the initial system outperforms this slightly since the noise is mostly white down to 300 s, allowing the necessary performance to be obtained by averaging.

V. Ratiometric Temperature Measurement

A common way of measuring temperatures is through the use of PT100 resistive thermometers. These resistors are platinum resistors, precision made to have a resistance of 100 Ω at $0°C$ and to then have a linear increase with temperature (here 0.385 Ω/K). This property allows a calculation of the temperature to be made once the resistance is measured as demonstrated in equation 3.

$$T = \frac{R_{measured} - 100}{0.385} \tag{3}$$

where T is in $°C$, $R_{measured}$ is in Ω.

One technique to measure resistance is the 4-wire measurement, which offers more advantages compared to the 2-wire measurement. The 2-wire measurement involves the measurement of a voltage over a resistor when applying a constant current, however, fluctuations in the current will cause changes in the measured voltage and appear to be a fluctuation in temperature. To combat this, a voltage can be applied to two resistors in series, one PT100 and a stable bias resistor. This stable bias resistor has a thermal coefficient of 50 parts per billion (ppb), meaning a 10 kΩ resistor would change by 0.5 mΩ with a 1 K change in temperature. When a measurement is made, it is always done as the ratio of the voltage drops over each resistor. This would cancel any

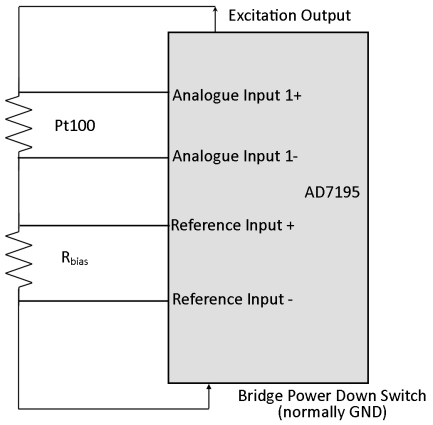

Fig. 7. An example of a ratiometric measurement. A voltage is applied to one side of two resistors in series allowing the AD7195 to measure the voltage drop across each. Due to one of the resistors in the bridge being thermally stable this allows a calculation of the resistance to be measured. The output from the AD7195 would be the ratio of the two resistances, thus multiplying by the bias resistors resistance, a value of the PT100 is obtained allowing the temperature to be found using equation 3.

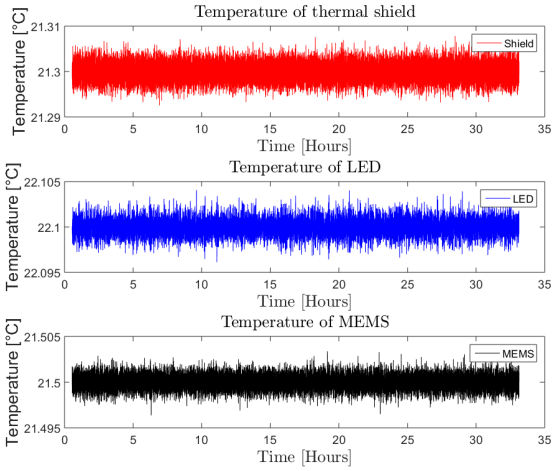

Fig. 8. Three graphs showing the temperature stability of the Shield (Top), LED (Middle) and MEMS (Bottom) over ≈ 30.5 hours. The largest variations are in the shield, which is the hardest to control, and are at $\approx \pm 5$ mK whereas the LED and MEMS vary by $\approx \pm 2$ mK.

current/voltage noise due to it being in common mode. This is known as a 4-wire measurement or ratiometric measurement. The simplified scheme is presented in figure 7. It also has an added advantage that any resistances in the wires used are also cancelled to a large degree.

Here, an AD7195 [34] was used due to its ability to not only automatically calculate the ratiometric measurement, but also to output an AC excitation and internally switch inputs so that valid data is converted. This AC excitation removes effects such as bridge potentials that occur when a DC current is used. These bridge potentials can offset the data, resulting in a misleading value of temperature, as well as drifts in the data. The result from the AD7195 which is the ratio of the PT100 and the bias resistor, is converted to a resistance of the PT100 by multiplying it by the resistance of the bias resistor, i.e. 10 kΩ. Since the resistance of the PT100, is around 100 Ω, which is a factor of 100 lower than the bias resistor, this allowed a gain of 64 to be utilised on the AD7195s to obtain an improved noise performance on the input signal.

A. Temperature Measurement Noise

There are several sources of error in measuring a temperature. Though the effect is small, the resistance of the bias resistor can still change due to temperature, which would be observed as a change in measured temperature. For a bias resistor with a thermal coefficient of 50 ppb, this would mean a 1 K change in temperature would also change the signal by 50 ppb. This 50 ppb would result in approximately a 5.4 $\mu\Omega \equiv 14$ μK error in the PT100 measurement. This is negligible under most circumstances, even if the temperature changes by 20 K, as other sources of noise exceed this value. The input of the AD7195 also introduces an error of 3 bits peak to peak at a gain of 64 and a sampling rate of 4.7 Hz (as stated in page 14 of datasheet [34]). A 3 bit error on the input is the equivalent of 8 in decimal which is the same as 4.8 mΩ. 4.8 mΩ is the equivalent of 12.4 mK pre-filtered. Using the same simulation used for shot noise, an estimate of the shot noise after filtering can be made. Here, 12.4 mK peak to peak input noise results in $\approx$ 1.4 mK peak to peak after three stages of decimation.

B. Temperature Control

The values obtained from the temperatures are then filtered and decimated to obtain an update period of $\approx 1 \rightarrow 3$ s. These can then be used in a control system such as a proportional, integral and differential (PID) that is currently used [35]. This PID is external to the board, it is operated from the PC software with which the board communicates. This will later be added as a function onto the firmware of the board. The PID control allows multiple temperatures to be simultaneously controlled (as seen in figure 8), where two temperatures, the MEMS, and LED are controlled to within ± 2 mK, and the outer shield that helps thermally insulate the device to ± 5 mK over a day. The shield is more difficult to control as its larger surface area can couple easier to the steel vacuum system (which is not thermally isolated) whereas the LED and MEMS are being thermally controlled inside the shield. Though no rigorous testing of the temperature limits have been done, an estimate for the temperature limits can be made. The stable bias resistors have a thermal coefficient of 50 ppb. Therefore to get a 2 mK change in signal, a 72 mΩ change in bias resistance is needed. This is the equivalent of 7.2 ppm, or a change in 144 K assuming the thermal coefficient is constant. This is not the case and in fact the thermal coefficient gets worse the further from room temperature they are. This estimate also ignores all other components such as the ADC and operation amplifiers used.

It can be seen from figure 9 that on decreasing the gain from the optimal value of 64, increases the noise on the measurements. The changing of the gain implies

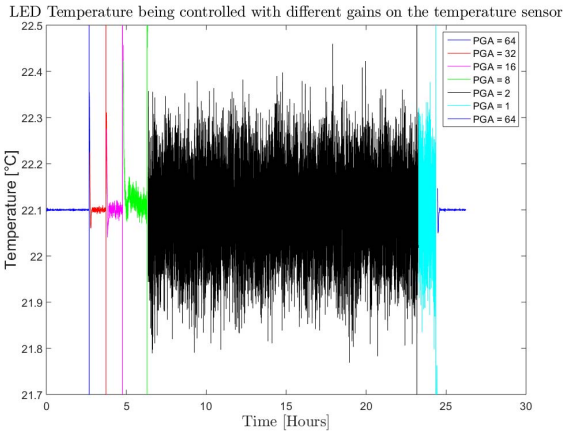

Fig. 9. Comparison of the LED temperature when using different gains on the AD7195 input. It shows that decreasing the gain increases the noise on the control due to the system being limited by the input noise of the ADC.

that the system is limited purely by the input noise of the AD7195.

VI. Tilt Sensors

As the MEMS [11] is measuring the vertical component of gravity, any tilt off-axis of the proof mass relative to the direction of gravity will change the measured output of the device. This makes tilt an important variable to monitor. The variation in acceleration sensitivity is given by equation 4.

$$x = \frac{g\cos\theta}{\omega^2} \tag{4}$$

where x is the displacement of the MEMS proof mass in m, g is the gravitational acceleration felt by the MEMS proof mass in m s^{-2}, ω is the resonant angular frequency of the device in rad s^{-1} and θ is the angle relative to the vertical direction, i.e. if $\theta = 0$, we would get 1 g of acceleration. By considering changes in g from changes in θ, the equation $\Delta g = \frac{-g\sin\theta}{\omega^2}\Delta\theta$ is obtained. It would be assumed that for small θ the device is insensitive to changes in tilt. This, however, is why it is more meaningful to consider $\cos\theta_2 - \cos\theta_1$ (where θ_1 and θ_2 are the angle going from some angle 1 to angle 2) instead of the $\sin\theta$ as even small changes in tilt close to zero will cause a change in the MEMS. Because of the $\sin\theta$ relationship, the MEMS is generally operated at vertical to minimise the tilt sensitivity, however, the MEMS can be designed and operated at almost any angle.

Using the outputs from the dsPIC itself to obtain high switching rates, an anti-phase oscillating signal is passed into two inputs of the electrolytic tilt sensor, SH50055-A-009 [36]. This anti-phase configuration (presented in figure 11) gives an output that oscillates between the voltage over one side of the electrolytic tilt sensor, then the other, allowing a difference of the sides to be taken. This difference is calculated digitally by the micro-controller after it is digitised, using an ADC internal to the dsPIC to sample. The difference between the voltage during high and low state is a measurement of the difference in impedance of each side of the bridge. This difference in impedance relates to the angle of the sensor from being level,

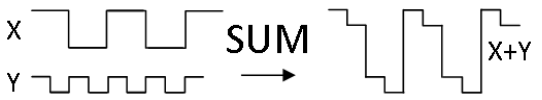

Fig. 10. Figure shows the excitation used for each tilt axis, X and Y, and what shape the data takes when combining each of the components. X and Y are summed together and sampled by an ADC at each of the four phases and allows each of the axes to be extracted from a single input. The figure gives an example where the tilt is larger in X than Y, which, can also be extracted from the the right when comparing the amplitude of modulation of each of the frequency components.

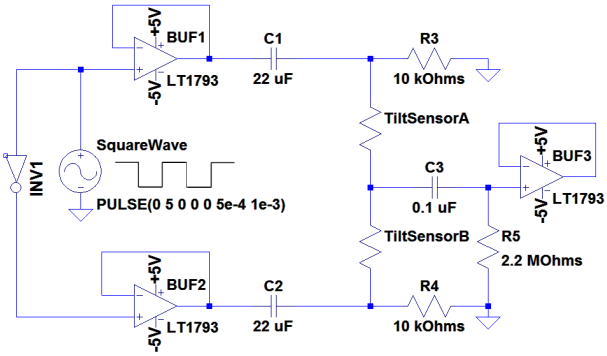

Fig. 11. Schematic diagram for running the Spectron electrolytic tilt sensors (the SH50055-A-009). An anti-phase drive is produced from the micro-controller's digital outputs to produce a voltage difference over the tilt sensor inputs. The output sees the voltage over one of the resistors during one half of a cycle and the other during the second. Taking the difference of these voltages gives a value based on how far its been tilted, i.e. the resistance of each side changes with tilt. This circuit is replicated for the other axis of measurement but with a square wave of twice the frequency. These components are summed together and read by an internal ADC on the micro-controller. Each component can be extracted as information on which part of the cycle is known by the micro-controller.

where zero difference between the high and low state would be measured when level. Figure 11 demonstrates the complete circuit for one axis, another copy of this circuit is required for the other axis but is modulated with a square wave of twice the frequency. These two axis outputs are then summed together before being sampled by the internal ADC of the dsPIC. Each axis can then be extracted from the single value by examining the phase each frequency component is at when sampling (seen in equation 5).

$$V_X = \frac{(V_1 + V_2) - (V_3 + V_4)}{2} \tag{5a}$$

$$V_Y = \frac{(V_1 + V_3) - (V_2 + V_4)}{2} \tag{5b}$$

where V_X and V_Y are the voltage relating to the tilt of each axes respectively and V_n is the voltage measured by the ADC during a four phase output cycle. Here axis Y is sampled at twice the frequency of X and this is illustrated in figure 10. The figure shows a small tilt in the Y axis being summed onto a larger tilt in the X axis.

For every 1 μrad; 2.2 mV is obtained, i.e. 2.2 V/mrad. This allows for a calibration of the tilt sensitivity by tilting it through a known amount and monitoring how much the output of the signal changes. The MEMS proof mass has a tilt sensitivity of 4.4 μGal/μrad. This requires the changes in tilt to be less than ≈ 9 μrad to get the desired 40 μGal sensitivity.

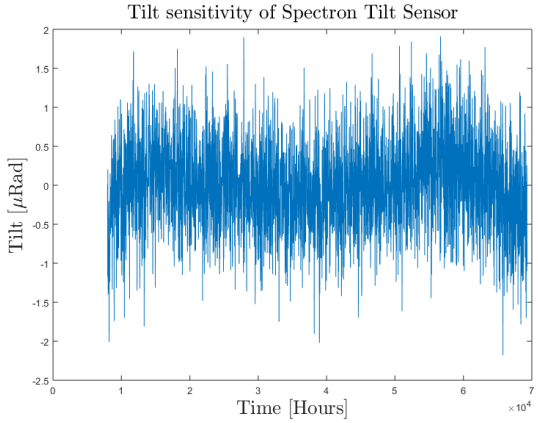

Fig. 12. Figure shows a maximum change of ≈ 2 μrad over ≈ 16.7 hours. This data has had offset, linear and 2nd order polynomial drift removed using a regression.

Figure 12 demonstrates a stability of ± 1 μrad allowing accurate enough monitoring.

VII. Conclusion

A highly stable optical shadow sensor has been demonstrated along with its digital readout and control. The system is shown to be able to measure displacements with a sensitivity of 0.6 nm over an integration time of 1000 s, whilst maintaining this sensitivity over periods of a day or longer. All functionality is obtained from a micro-controller-based, custom electronics board. This electronics board can measure and control several temperatures to ± 2 mK; monitor changes in tilt to ± 1 μrad; power and modulate an LED; convert μA of current to measurable voltages; demodulate a digitised signal; compute digital filters; and decimate the output signals. Whilst the shadow sensor has been designed for us in a low-cost portable MEMS gravimeter, the sensor could be re-purposed to serve in many precision sensing applications.

References

[1] N. A. Lockerbie and K. V. Tokmakov, "A 'Violin-Mode'shadow sensor for interferometric gravitational wave detectors," *Meas. Sci. Technol.*, vol. 25, no. 12, p. 125110, 2014.

[2] D. H. A. Munap, N. Bidin, S. Islam, M. Abdullah, F. Marsin, and M. Yasin, "Fiber optic displacement sensor for industrial applications," *IEEE Sensors J.*, vol. 15, no. 9, pp. 4882–4887, Sep. 2015.

[3] J. A. Mulligan, G. R. Untracht, S. N. Chandrasekaran, C. N. Brown, and S. G. Adie, "Emerging approaches for high-resolution imaging of tissue biomechanics with optical coherence elastography," *IEEE J. Sel. Topics Quantum Electron.*, vol. 22, no. 3, pp. 246–265, May 2016.

[4] S. Zhong and Q. Zhang, "Enhanced optical coherence vibration tomography for subnanoscale-displacement-resolution calibration of piezoelectric actuators," *Sens. Actuators A, Phys.*, vol. 233, pp. 42–46, Sep. 2015. [Online]. Available: http://www.sciencedirect.com/science/article/pii/S0924424715300492

[5] I. Levental *et al.*, "A simple indentation device for measuring micrometer-scale tissue stiffness," *J. Phys. Condens. Matter*, vol. 22, no. 19, p. 194120, 2010.

[6] C. Steffens, F. L. Leite, C. C. Bueno, A. Manzoli, and P. S. De Paula Herrmann, "Atomic force microscopy as a tool applied to nano/biosensors," *Sensors*, vol. 12, no. 6, pp. 8278–8300, 2012.

[7] T. Ando, T. Uchihashi, and T. Fukuma, "High-speed atomic force microscopy for nano-visualization of dynamic biomolecular processes," *Prog. Surf. Sci.*, vol. 83, nos. 7–9, pp. 337–437, 2008, doi: http://dx.doi.org/10.1016/j.progsurf.2008.09.001

[8] S. Cho, J. F. Cárdenas-García, and I. Chasiotis, "Measurement of nanodisplacements and elastic properties of MEMS via the microscopic hole method," *Sens. Actuators A, Phys.*, vol. 120, no. 1, pp. 163–171, 2005.

[9] M. Podhraški and J. Trontelj, "A differential monolithically integrated inductive linear displacement measurement microsystem," *Sensors*, vol. 16, no. 3, p. 384, 2016.

[10] S. Fericean, A. Hiller-Brod, A. D. Dorneich, and M. Fritton, "Microwave displacement sensor for hydraulic devices," *IEEE Sensors J.*, vol. 13, no. 12, pp. 4682–4689, Dec. 2013.

[11] R. P. Middlemiss, A. Samarelli, D. J. Paul, J. Hough, S. Rowan, and G. D. Hammond, "Measurement of the Earth tides with a MEMS gravimeter," *Nature*, vol. 531, no. 1, p. 614–617, Mar. 2016. [Online]. Available: https://www.nature.com/articles/nature17397

[12] P. Campsie, G. D. Hammond, R. P. Middlemiss, D. J. Paul, and A. Samarelli, "Measurement of acceleration," WO Patent 030 435 A1, Mar. 3, 2016.

[13] R. Middlemiss, "Practical MEMS gravimeter," Ph.D. dissertation, Inst. Gravitational Res., Univ. Glasgow, Scotland, U.K., 2016.

[14] D. P. Blair and P. H. Sydenham, "Phase sensitive detection as a means to recover signals buried in noise," *J. Phys. E, Sci. Instrum.*, vol. 8, no. 8, p. 621, 1975.

[15] M. O. Sonnaillon and F. J. Bonetto, "A low-cost, high-performance, digital signal processor-based lock-in amplifier capable of measuring multiple frequency sweeps simultaneously," *Rev. Sci. Instrum.*, vol. 76, no. 2, p. 024703, 2005.

[16] L. E. Bengtsson, "A microcontroller-based lock-in amplifier for sub-milliohm resistance measurements," *Rev. Sci. Instrum.*, vol. 83, no. 7, p. 075103, 2012.

[17] S. Carrato, G. Paolucci, R. Tommasini, and R. Rosei, "Versatile low-cost digital lock-in amplifier suitable for multichannel phase-sensitive detection," *Rev. Sci. Instrum.*, vol. 60, no. 7, p. 2257, 1989.

[18] J. Leis, P. Martin, and D. Buttsworth, "Simplified digital lock-in amplifier algorithm," *Electron. Lett.*, vol. 48, no. 5, pp. 259–261, Mar. 2012.

[19] M. Sonnaillon, R. Urteaga, F. J. Bonetto, and M. Ordonez, "Implementation of a high-frequency digital lock-in amplifier," in *Proc. Can. Conf. Elect. Comput. Eng.*, May 2005, pp. 1229–1232. [Online]. Available: http://ieeexplore.ieee.org/document/1557199/

[20] D. Wu, C. Wang, H. Sun, and H. Wang, "A novel digital lock-in amplifier with dual channels," in *Proc. Int. Asia Conf. Inform. Control, Autom., Robot. (CAR)*, vol. 1. Feb. 2009, pp. 464–468.

[21] A. A. Dorrington and R. Kunnemeyer, "A simple microcontroller based digital lock-in amplifier for the detection of low level optical signals," in *Proc. 1st IEEE Int. Workshop Electron. Design, Test Appl.*, Jan. 2002 pp. 486–488.

[22] J. Aguirre, N. Medrano, B. Calvo, and S. Celma, "Lock-in amplifier for portable sensing systems," *Electron. Lett.*, vol. 47, no. 21, pp. 1172–1173, Oct. 2011.

[23] Microchip. *16-Bit Microcontrollers and Digital Signal Controllers with High-Speed PWM, USB and Advanced Analog*. Accessed: Aug. 16, 2017. [Online]. Available: http://ww1.microchip.com/downloads/en/DeviceDoc/70616g.pdf

[24] D. Wenn, "Implementing digital lock-in amplifiers using the dsPIC DSC," Microchip, Tech. Rep. AN115, 2007, pp. 1–12. [Online]. Available: http://www.microchip.com/wwwAppNotes/AppNotes.aspx?appnote=en532447

[25] Laser Components. *LIA-MVD-200-L Data Sheet*. Accessed: Aug. 16, 2017. [Online]. Available: https://www.lasercomponents.com/fileadmin/user_upload/home/Datasheets/femto/lock-in/lia-mvd-200-l.pdf

[26] R. P. Middlemiss *et al.*, "Field tests of a portable MEMS gravimeter," *Sensors*, vol. 17, no. 11, p. 2571, 2017.

[27] A. Zoellner, E. Hultgren, and K.-X. Sun. (2013). "Integrated differential optical shadow sensor for modular gravitational reference sensor." [Online]. Available: https://arxiv.org/abs/1302.1623

[28] A. Zoellner *et al.*, "Differential optical shadow sensor for sub-nanometer displacement measurement and its application to drag-free satellites," *Opt. Exp.*, vol. 25, no. 21, pp. 25201–25211, Oct. 2017. [Online]. Available: http://www.opticsexpress.org/abstract.cfm?URI=oe-25-21-25201

[29] Texas Instruments. *ADS1248 Data Sheet*. [Online]. Available: http://www.ti.com/lit/ds/symlink/ads1248.pdf

[30] G. Vasilescu, *Electronic Noise and Interfering Signals*. Springer, 2005. [Online]. Available: http://www.springer.com/us/book/9783540407416 and https://link.springer.com/book/10.1007%2Fb137720

[31] Texas Instruments. *TLV5616 Data Sheet*. Accessed: Aug. 16, 2017. [Online]. Available: http://www.ti.com/lit/ds/symlink/tlv5616.pdf

[32] D. K. Lindner, *Introduction to Signals and Systems*. New York, NY, USA: McGraw-Hill, 1999. [Online]. Available: https://books.google.co.uk/books/about/Introduction_to_Signals_and_Systems.html?id=n8KhGQAACAAJ&redir_esc=y
[33] Microchip. *dsPIC33E/PIC24E Family Reference Manual: Section 2. CPU*. Accessed: Aug. 16, 2017. [Online]. Available: http://ww1.microchip.com/downloads/en/DeviceDoc/S2.pdf
[34] Analog Devices. *AD7195 Data Sheet*. Accessed: Aug. 16, 2017. [Online]. Available: http://www.analog.com/media/en/technical-documentation/data-sheets/AD7195.pdf
[35] K. J. Åström and R. M. Murray, *Feedback Systems, Version 2.10b ed.*. Princeton, NJ, USA: Princeton Univ. Press, Feb. 2009. [Online]. Available: http://www.cds.caltech.edu/~murray/books/AM05/pdf/am08-complete_22Feb09.pdf
[36] Spectron Sensors. *Electrolytic Tilt Sensors—SH50050 Ceramic Series*. Accessed: Aug. 16, 2017. [Online]. Available: http://www.spectronsensors.com/datasheets/SDS-116-3106.pdf

Steven G. Bramsiepe was born in Dumfries, Scotland, in 1990. He received the M.Sc. degree in physics from the University of Glasgow, Glasgow, Scotland, in 2013, where he is currently pursuing the Ph.D. degree with the Center for Doctoral in Intelligent Sensing and Measurement, Institute of Gravitational Research. His work interests include low noise electronics, precision measurements, and gravimetery and its uses.

David Loomes received the degree in electronics and electrical engineering in 1983. He has been involved in developing embedded control and instrumentation systems since 1983. His particular areas of interest include semi-conductor manufacturing and motor-sport oriented systems.

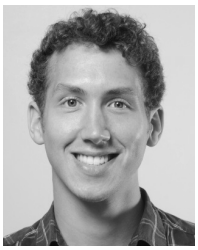

Richard P. Middlemiss received the Ph.D. degree from the Institute for Gravitational Research in 2016. He is currently a Research Associate with the University of Glasgow. His interests include MEMS gravimeters, nanofabrication techniques, volcano gravimetry, and the dissemination of science to the public.

Douglas J. Paul (M'00–SM'05) is currently a Professor of Semiconductor Devices at Glasgow and was the Director of the James Watt Nanofabrication Centre from 2010 to 2015. He currently has an EPSRC Quantum Technology Fellowship and received the Institute of Physics President's Medal in 2014. His research includes nanofabrication, nanoelectronics, Si photonics, energy harvesting, and quantum technology.

Giles D. Hammond is currently a Professor of Experimental Gravitational Physics with the University of Glasgow. His research includes the development/installation/commissioning of the fused silica suspensions for the aLIGO gravitational wave detectors, together with activities focused on MEMS gravimeters, and integrated silicon interferometers.